

rogamy (Fig. 2) and conventional or reversed SSD (Fig. 5) must necessarily be made at bifurcating nodes. Where multiple nodes (consisting of sister taxa exhibiting, for example, all conventional SSD) made up one side of the node, the mean value of their individual SSD scores was used in the contrast against the taxa exhibiting reversed SSD, at that particular node.

33. A. Grafen, *Philos. Trans. R. Soc. London Ser. B* **326**, 119 (1989).

34. We are grateful to I. Owens, A. Read, M. Zuk, and three anonymous reviewers for commenting on and improving earlier drafts of this manuscript, and to R. Johnstone and I. Owens for providing valuable guidance on the CAIC analyses. We also acknowledge the help of S. Cotter, R. Hails, C. Lapsley, and D. Promislow. The authors declare that there was no sex bias in the contributions made to this paper. Supported by the Natural Environment Research Council, UK.

#### Supporting Online Material

[www.sciencemag.org/cgi/content/full/297/5589/2015/DC1](http://www.sciencemag.org/cgi/content/full/297/5589/2015/DC1)

Materials and Methods

SOM Text

Figs. S1 and S2

References and Notes

21 May 2002; accepted 25 July 2002

## Nucleotide Control of Interdomain Interactions in the Conformational Reaction Cycle of SecA

John F. Hunt,<sup>1,2\*†</sup> Sevil Weinkauf,<sup>2,3\*</sup> Lisa Henry,<sup>2</sup> John J. Fak,<sup>1\*</sup> Paul McNicholas,<sup>4\*</sup> Donald B. Oliver,<sup>4</sup> Johann Deisenhofer<sup>2</sup>

The SecA adenosine triphosphatase (ATPase) mediates extrusion of the amino termini of secreted proteins from the eubacterial cytosol based on cycles of reversible binding to the SecYEG translocon. We have determined the crystal structure of SecA with and without magnesium–adenosine diphosphate bound to the high-affinity ATPase site at 3.0 and 2.7 angstrom resolution, respectively. Candidate sites for preprotein binding are located on a surface containing the SecA epitopes exposed to the periplasm upon binding to SecYEG and are thus positioned to deliver preprotein to SecYEG. Comparisons with structurally related ATPases, including superfamily I and II ATP-dependent helicases, suggest that the interaction geometry of the tandem motor domains in SecA is modulated by nucleotide binding, which is shown by fluorescence anisotropy experiments to reverse an endothermic domain-dissociation reaction hypothesized to gate binding to SecYEG.

SecA uses ATP-driven cycles of insertion and retraction from the membrane-bound SecYEG translocon to mediate processive extrusion of preproteins through the cytoplasmic membrane of eubacteria (1–4). This cyclical interaction explains the presence of SecA in vivo in both soluble and membrane-bound forms (5). In vitro translocation assays show that the ATPase activity of SecA (6, 7) is required for the transmembrane transport of the NH<sub>2</sub>-terminus of the preprotein, which includes the signal sequence (8, 9) that targets proteins for export through the translocon (3, 10). The ATPase activity of SecA is also

required to drive the transport of downstream COOH-terminal segments of the preprotein in the absence of a transmembrane proton-motive force (10–12). Understanding the structure of SecA and its ATP-driven conformational reaction cycle is essential to understanding the mechanism by which the energy of ATP binding and hydrolysis is exploited to produce vectorial preprotein transport.

**Crystal structure determinations and refinements.** The soluble form of SecA from *Bacillus subtilis* was crystallized (13) and solved (14) in space group *P*<sub>3</sub>12. Multiple isomorphous replacement phases were obtained to 4.4 Å by using heavy-atom derivatives of wild-type protein and an N96C mutant. The phases were extended to high resolution by using density modification procedures (15) combined with partial-model building. Assignment of the sequence was facilitated by the use of an anomalous difference Fourier map from a selenomethionine derivative that showed the locations of 33 of the 36 methionines, and a real-space cross-validation procedure was used when adding the side chains to prevent phase bias from impeding the procedure. Because the refined phases are ultimately derived from the coordinate model in all macromolecular crystal structure determinations, the quality of the map (fig. S1) (14) and of the model (Table 1 and Fig. 1) produced in this way is equivalent to that

of a structure solved in a more traditional way and refined to an equivalent *R* factor.

SecA crystallized isomorphously either in the presence or absence of adenine nucleotides or analogs, consistent with solution studies showing that nucleotide binding does not produce large conformational changes in the free enzyme (16). Isomorphous difference Fourier maps from all nucleotide-containing crystals showed electron density for a single ligand bound at the high-affinity ATPase site identified in mutagenesis studies (17). Slightly weaker diffraction (by ~0.5 Å) was obtained when nucleotides were cocrystallized rather than soaked in after growth, so that we chose to refine a data set obtained from a native crystal soaked in 5 mM Mg-ATP for 2.5 hours. However, there was no evidence of the  $\gamma$ -phosphate of ATP during the subsequent refinement, indicating that Mg-ADP was bound. Additional soaking experiments suggested that a kinetic barrier prevents Mg-ATP binding in the crystal lattice (18). Given the high affinity of SecA for Mg-ADP [dissociation constant (*K*<sub>d</sub>) ≈ 100 nM] (19), we assume that the protein selectively bound the low concentration of Mg-ADP in the stock.

There was no credible evidence for a second bound nucleotide molecule in the refined Mg-ADP-bound structure, indicating that the low-affinity ATP-binding site (17, 20) was not stably occupied by well-ordered nucleotide in our crystals. Binding could have been inhibited by the >2 M NH<sub>2</sub>(SO<sub>4</sub>)<sub>2</sub> present in the mother liquor or prevented by crystal packing interactions, which could either obstruct the site or restrain the protein in an incompatible conformation. (General considerations concerning the potential location of this site are presented in the SOM text.)

The apo structure was refined (21) at 2.7 Å resolution to working and free *R* factors of 22.1 and 30.4%, respectively, whereas the Mg-ADP-bound structure was refined at 3.0 Å resolution to working and free *R* factors of 21.8 and 29.4%, respectively (Table 1 and Fig. 1; figs. S2 and S3). The same set of free reflections was used for both refinements. Only ~83% of the residues in the refined SecA structures have most-favored Ramachandran angles. However, there are very few Ramachandran outliers, and the residues with noncore angles occur primarily in weakly ordered regions with very high backbone *B* factors. The well-ordered regions have good backbone geometry, and the low root-

<sup>1</sup>Department of Biological Sciences, 702A Fairchild Center, MC2434, Columbia University, New York, NY 10027, USA. <sup>2</sup>Howard Hughes Medical Institute and Department of Biochemistry, The University of Texas Southwestern Medical Center, 5323 Harry Hines Boulevard, Dallas, TX 75390–9050, USA. <sup>3</sup>Department of Chemistry, Technical University Munich, Lichtenbergstrasse 4, D-85748 Garching, Germany. <sup>4</sup>Department of Molecular Biology and Biochemistry, Lawn Avenue, Wesleyan University, Middletown, CT 06459, USA.

\*Present addresses: Columbia University, New York, NY 10027, USA. (J.F.H.); Technical University Munich, Lichtenbergstrasse 4, D-85748 Garching, Germany (S.W.); Laboratory of Developmental Neurogenetics, Rockefeller University, New York, NY 10021, USA (J.J.F.); Schering-Plough Research Institute, Kenilworth, NJ 07033, USA (P.M.).

†To whom correspondence should be addressed. E-mail: hunt@sid.bio.columbia.edu

mean-square deviations (rmsd's) of bond lengths and angles (Table 1) indicate excellent overall geometry.

The electron density in the weakly ordered regions of SecA was difficult to interpret even after convergence of the refinement. Based on inspection of composite simulated-annealing omit maps (21), 148 of the 802 residues in the protein model have been designated "unreliable" and marked with a "U" in the final row of the sequence alignment blocks in fig. S3. Representative electron density from the best and worst regions of these omit maps is shown in fig. S1. The unreliable residues are all located in regions with very high backbone *B* factors. However, the high quality of the model elsewhere and the correctness of the overall chain trace in the weakly ordered regions is supported by several factors: (i) the *R* factors of the refined models; (ii) analyses of the composite omit maps (21); (iii) the identical topology of the motor domains in SecA and those in superfamily-II (SF-II) helicases even though they were traced independently; and (iv) the ability to account for the 33 methionine sites in an anomalous difference Fourier map from a selenomethionine derivative (14).

#### Structural similarity of the motor domains to those in SF-I and -II helicases.

The crystal structure of soluble SecA shows extensive packing interactions between the five ordered domains in the protomer (Fig. 1). A topology diagram of the molecule is presented in fig. S2. As predicted on the basis of sequence analysis (22, 23), the core of SecA comprises a pair of F1-type nucleotide-binding folds (Fig. 2, A and B) resembling the tandem motor domains in SF-I and -II ATP-dependent helicases (24–26). A structure-sequence alignment that includes a set of helicases is shown in fig. S3. These two domains, designated NBF-I and NBF-II (nucleotide-binding folds I and II), are shown in dark and light blue, respectively. NBF-I is the most well ordered domain in the structure, with a mean backbone *B* factor of 50 Å<sup>2</sup>. NBF-II is more weakly ordered with a mean backbone *B* factor of 86 Å<sup>2</sup>, and the distribution of *B* factors within NBF-II suggests that it pivots about its point of attachment to NBF-I. As in the related helicases, the high-affinity ATP-binding site in SecA is located at this interface between NBF-I and NBF-II (Fig. 1), with most of the contacts to the nucleotide coming from the "helicase motifs" (22, 24) (Fig. 2C). The primary role of nucleotide binding in homologous mechanoenzymes is probably to control the packing angle between NBF-I and NBF-II (see below).

NBF-I and NBF-II in SecA have the same protein fold (fig. S2 and Fig. 2B) except for the substitution of a meander in NBF-II for the  $\alpha$  helix connecting  $\beta$  strands 4 and 5 and the substitution of an antiparallel for a parallel  $\beta$  strand at position 7 in the  $\beta$  sheets (fig. S2). The

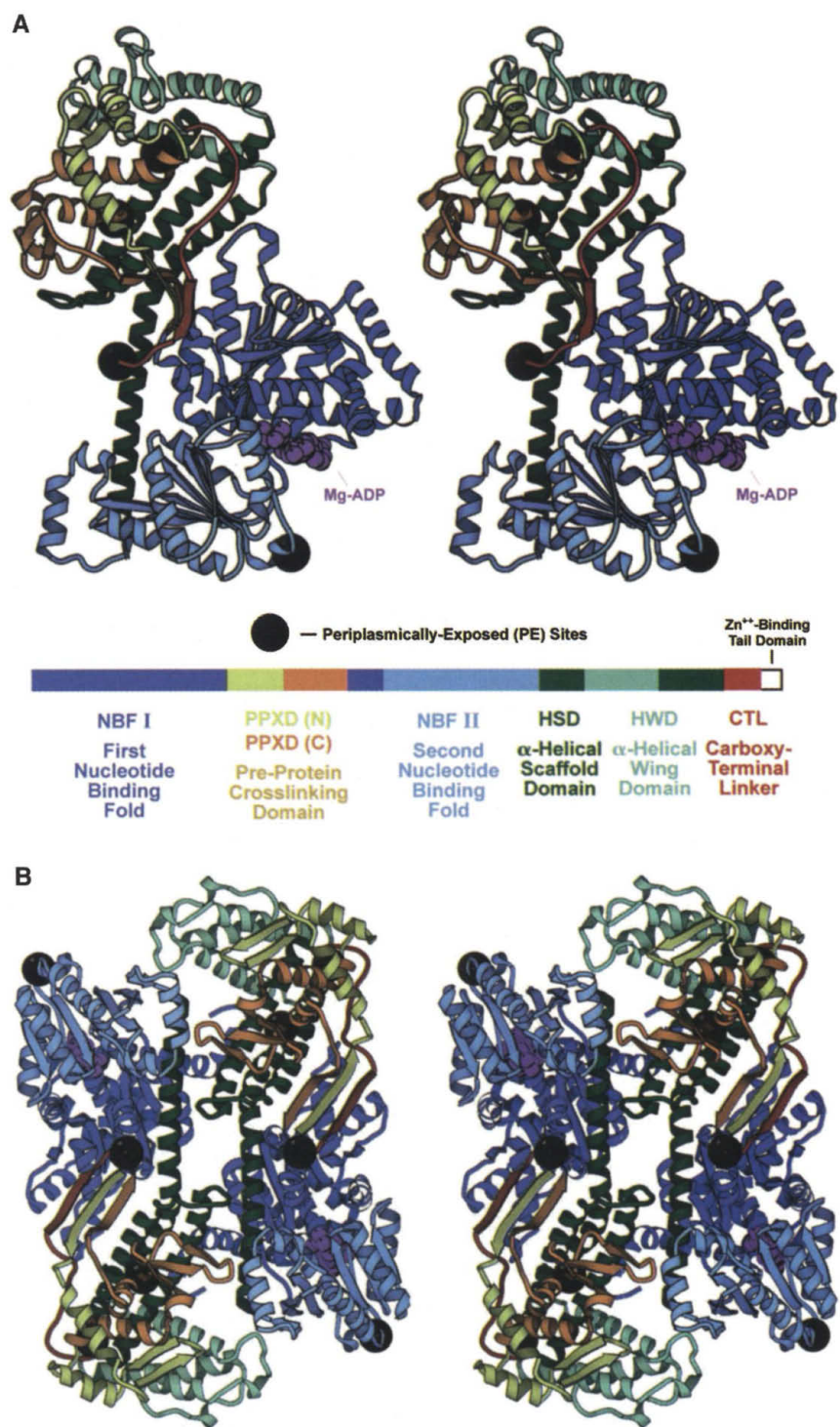


**Fig. 1.** The crystal structure of the SecA translocation ATPase from *B. subtilis* colored according to domain organization. (A) Stereo ribbon diagram of the Mg-ADP-bound protomer. The bar at the bottom of this panel shows the locations of the protein domains in the linear sequence of SecA and defines the color coding. The black spheres represent positions that are exposed to the periplasm in SecYEG-bound SecA. A space-filling representation of the bound Mg-ADP molecule is shown in magenta. The first and second nucleotide-binding folds (NBF-I and NBF-II) are shown in dark and light blue, respectively; the NH<sub>2</sub>- and COOH-terminal regions of the preprotein-cross-linking domain [PPXD(N) and PPXD(C)] are shown in yellow and orange, respectively; the  $\alpha$ -helical scaffold domain (HSD) and  $\alpha$ -helical wing domain (HWD) are shown in dark and light green, respectively; and the COOH-terminal linker peptide (CTL) is shown in red. The final 39 residues are disordered in the crystal. The pair of  $\beta$  strands leading into and out of the PPXD are shown in yellow and orange in order to clarify the location of the PPXD; however, these  $\beta$  strands make extensive packing interactions with NBF-I and therefore structurally constitute part of NBF-I. (B) The likely physiological dimer of SecA formed by two subunits related by crystallographic symmetry.

central  $\beta$  sheets have the characteristic pattern of  $\beta$ -strand interdigitation (fig. S2 and Fig. 2A) observed in F1 ATPase (27) and a diverse set of related ATPases, including the RecA recombinase. While DALI (28) indicates highly significant  $Z$  scores of  $\sim 6$  for the alignment of either NBF in SecA with F1, consistently stronger structural similarity is observed to the tandem F1-like domains in the SF-I and -II helicases. Given the variability in the packing angle between these motor domains (25, 26, 29), it is difficult to simultaneously align both in comparing different structures. However, DALI gives better  $Z$  scores, ranging from 9 to 16 when the NBFs in SecA are compared individually with the corresponding domains in SF-I and -II helicases.

The strongest structural similarity is to the SF-II DEAD-box helicases MJ0660 (30) and eukaryotic initiation factor 4A (eIF4A) (31, 32). Least-squares superposition of NBF-I in SecA with the corresponding domain in eIF4A yields a 2.7 Å rmsd for 177 out of 196 C $\alpha$  atoms in the homologous region, whereas superposition of NBF-II yields a 2.6 Å rmsd for 125 out of 145 C $\alpha$  atoms. The NBFs of SecA also show strong similarity to the motor domains in the SF-II helicase UvrB [Protein Data Bank (PDB) accession number 1D2M] and only slightly weaker similarity to the SF-II helicase NS3 from the hepatitis C virus (PDB 1HEI) and the SF-I helicases PcrA and Rep (figs. S3 and S5).

**Domain organization of the remainder of the protomer.** The region identified as being required for cross-linking overlapping fragments of SecA to a model preprotein (11) forms a pair of closely associated subdomains, designated PPXD(N) and PPXD(C) [NH<sub>2</sub>- and COOH-termini of the preprotein cross-linking (x-linking) domain] that are shown in yellow and orange, respectively (Fig. 1 and elsewhere). Contrary to the assumption that this structure would be located after the end of NBF-I (17), the PPXD is inserted between  $\beta$  strands 5 and 6 in NBF-I. Both of its subdomains are weakly ordered but are distinguished by different mean backbone  $B$  factors: 129 Å<sup>2</sup> for PPXD(N) versus 87 Å<sup>2</sup> for PPXD(C). The PPXD shows at most weak structural similarity (28) to other proteins of known structure. Although the cross-linking studies establish the PPXD as a candidate site for preprotein binding, additional data supporting a direct interaction in this region are lacking. Nucleic acid-binding domains are inserted at an adjacent topological position in NBF-I of many SF-I and -II helicases (26).

The COOH-terminal  $\sim 30$  kD of SecA forms two  $\alpha$ -helical domains. One of these (shown in dark green) comprises a bundle of three antiparallel  $\alpha$  helices, with some structural similarity to  $\alpha$ -helical coiled-coils, that is almost as well ordered as NBF-I based on its mean backbone  $B$  factor (66 Å<sup>2</sup>). This domain,

designated the HSD ( $\alpha$ -helical scaffold domain), functions as a global conformational template. The NH<sub>2</sub>-terminal  $\alpha$  helix in the HSD stretches throughout most of the length of SecA, with one face making packing interactions with NBF-I and NBF-II (Fig. 1A) and the opposite face making packing interactions in the intersubunit interface of the physiological dimer (Fig. 1B). The COOH-terminal  $\alpha$  helices in the HSD bind the PPXD and thereby maintain its position relative to NBF-I and NBF-II. The second  $\alpha$ -helical domain (shown in light green) is inserted between  $\alpha$  helices 1 and 2 in the HSD (Fig. 1A and fig. S2) and is weakly attached to the core of SecA based on its high mean backbone  $B$  factor (99 Å<sup>2</sup>). This domain is designated the HWD ( $\alpha$ -helical wing domain). DALI (28) indicates that the HWD shows weak but significant structural similarity to an acyl carrier protein involved in polyketide synthesis (PDB accession number 2AF8;  $Z = 3.9$  with 2.4 Å rmsd for 59 of the 84 C $\alpha$ s in the HWD). The HWD combined

with regions of the HSD forms a 30-kD protease-resistant fragment when complexed with SecYEG (1, 33, 34).

The cysteine-rich COOH-terminal 22 residues of SecA form a Zn-binding domain that interacts with SecB and phospholipids (35–37). Although this domain is not observed in the crystal structure and is therefore disordered, 25 residues connecting it to the HSD (shown in red) are observed and have been designated the CTL (COOH-terminal linker). Part of the CTL forms a  $\beta$  strand bound to one edge of a small antiparallel  $\beta$  sheet comprising the  $\beta$  strands connecting NBF-I to the PPXD (Figs. 1A and 3C; fig. S2)

**The high-affinity ATPase site is formed by the helicase motifs.** NBF-I of SecA binds adenine nucleotides with a very similar geometry to F1 ATPase (27) (Fig. 2A). The Walker A consensus sequence (helicase motif I) forms the “P-loop” helix-capping structure that binds the  $\alpha$ - and  $\beta$ -phosphates of the nucleotide, and the Walker B consensus (he-

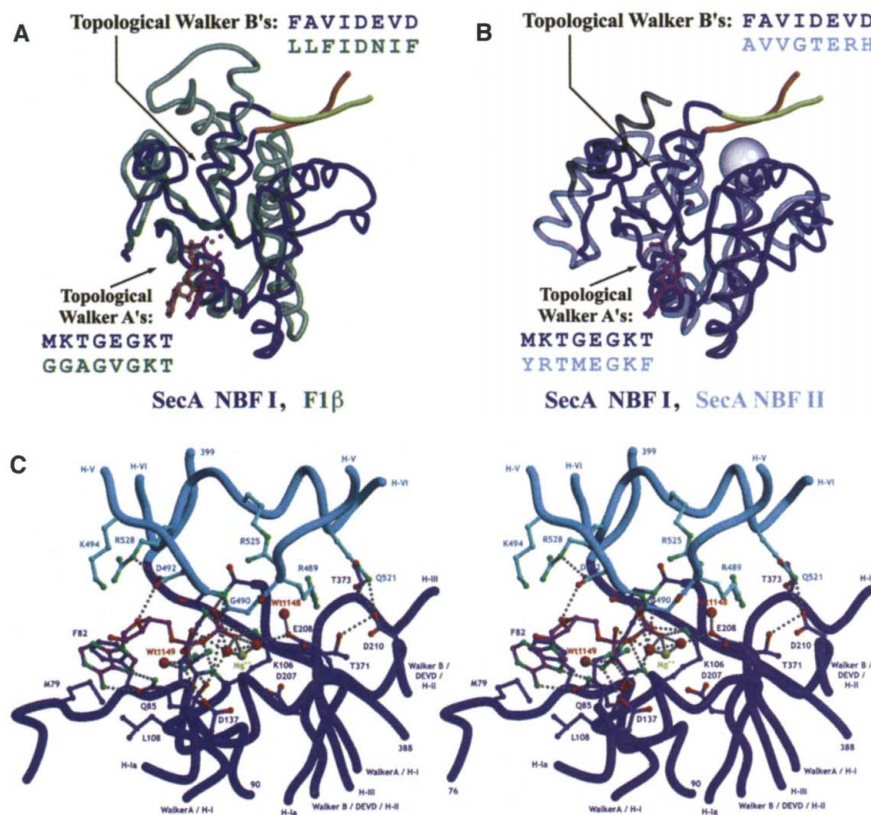


**Fig. 2.** The high-affinity ATP-binding site of SecA. (A) NBF-I of SecA (dark blue) is compared with the  $\beta$  subunit of bovine mitochondrial F1 ATPase (translucent green) (27) based on least-squares alignment of their central  $\beta$  sheets. The protein segments connecting NBF-I of SecA to the PPXD are shown in yellow and orange. The Mg-ADP ligands bound to NBF-I of SecA and F1 $\beta$  are shown in magenta and translucent red ball-and-stick representations, respectively. (B) NBF-I (dark blue) and NBF-II of SecA (translucent cyan) are compared in the same manner. The large sphere represents the location of the high-affinity nucleotide-binding site relative to NBF-II of SecA (i.e., adjacent to helicase motifs V and VI in NBF-II). (C) Stereo ribbon diagram of the active site in the Mg-ADP-bound structure. The locations of the helicase motifs (24, 26) are indicated (Walker A/H-I, H-Ia, Walker B/DEVD/H-II, H-III, H-V, H-VI). The backbone worm and most of the atoms in the side chains and ligand are colored according to the domain of origin, but oxygen atoms are shown in red, nitrogen atoms in light green, and the Mg<sup>2+</sup> ion in yellow. H-bonds are indicated by dashed gray lines.

licase motif II) forms a hydrophobic  $\beta$  strand that terminates in residue Asp-207, which contacts the  $Mg^{2+}$  cofactor (Fig. 2C and fig.

S4). This Asp is the first residue in the DEAD-box sequence (DEVD in SecA) that is found in a subclass of SF-II helicases but not

F1 (fig. S3). Glu-208 in the DEAD-box is the leading candidate to be the catalytic base in the ATP hydrolysis reaction because it makes a hydrogen bond (H-bond) to water 1148, which is positioned to make a hydrolytic attack on the  $\gamma$ -phosphate of ATP (Fig. 2C). The residues contacting the base of the nucleotide come primarily from the  $NH_2$ -terminus of  $\alpha$  helix 4 in NBF-I in a region that is not a helicase motif but is conserved in DEAD-box helicases (fig. S3).

The other direct contacts to the nucleotide are made by helicase motifs V and VI, which are located in a different region of NBF-II than the topological equivalents of the Walker A and B sequences (Fig. 2B and SOM text). Residues Gly-490, Asp-492, and Lys-494 in motif V contact the  $\alpha$ -phosphate and the ribose, while residue Arg-528 at the COOH-terminus of motif VI contacts the ribose and residue Asp-492 (Fig. 2C and fig. S4). Residue Gln-521 in motif VI forms a cooperative H-bonding network with three residues in NBF-I: Asp-210, at the COOH-terminus of the DEAD box in motif II; and Thr-371 and Thr-373 in motif III. The “arginine finger,” residue 525 in motif VI, is positioned to contact the  $\gamma$ -phosphate of the nucleotide when ATP is bound (Fig. 2C); such an interaction was observed in PcrA (29) but would not be possible in the nucleotide-free structure of MJ0669 (30) where a rigid-body rotation of NBF-I relative to NBF-II creates a major opening of the nucleotide-binding cleft (Fig. 4A).

**Locations of established periplasmically exposed sites.** The black spheres in Fig. 1 indicate the sites in *B. subtilis* SecA equivalent to those that are periplasmically exposed (PE) in membrane-bound *Escherichia coli* SecA based on topological mapping experiments conducted with chemical labeling in conjunction with cysteine-scanning mutagenesis (33, 38). The most strongly labeled PE site in *E. coli* SecA occurs in the Gram-negative-specific insertion in NBF-II, which is missing in *B. subtilis* SecA (fig. S3). This site is located on the surface near the high-

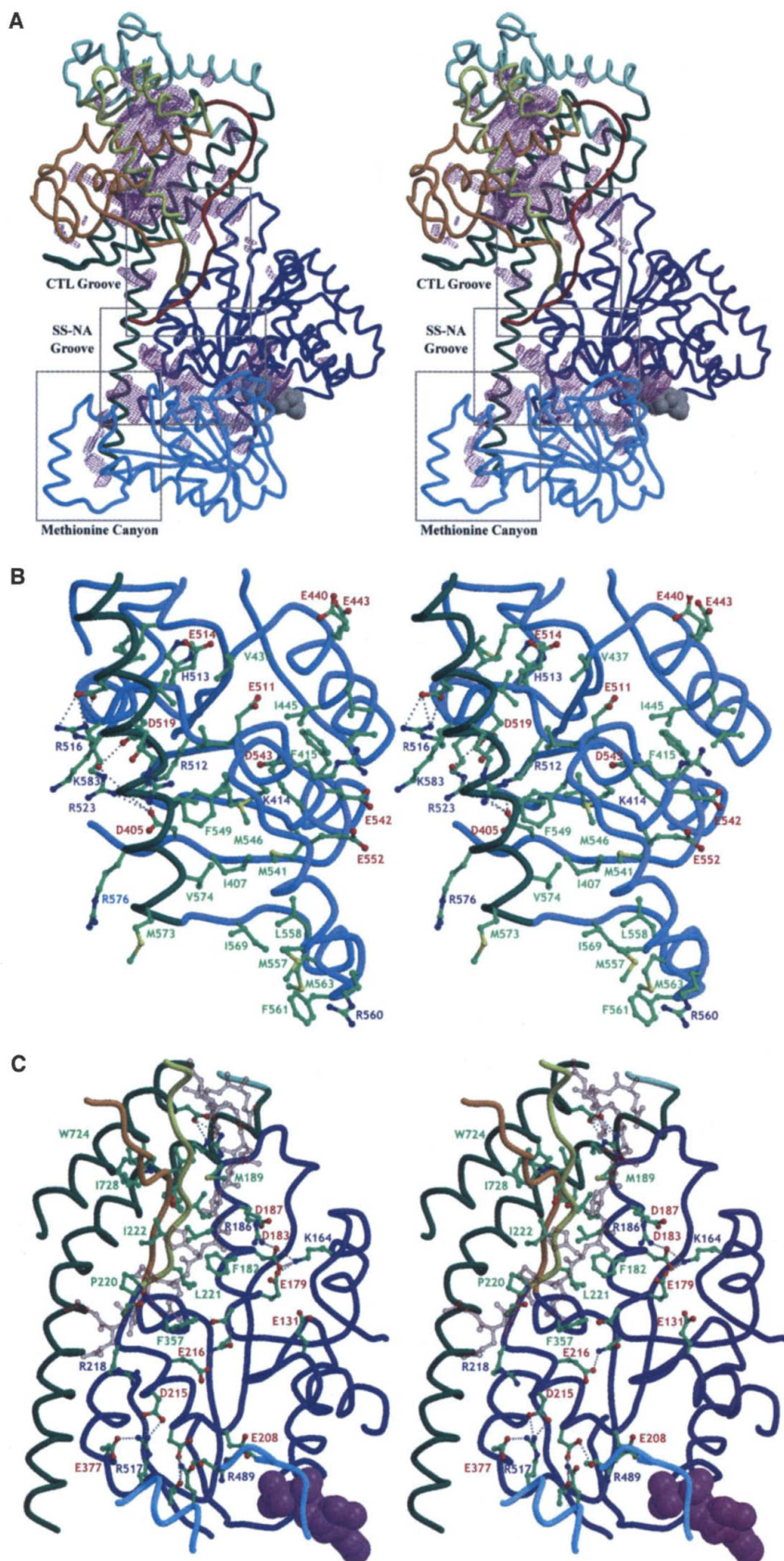


**Fig. 3.** Stereo ribbon diagrams showing locations of possible ligand-interaction sites in the SecA monomer. The backbone worms are colored according to domain organization. The bound Mg-ADP ligand is shown in space-filling representation in gray in (A) but in magenta in the other panels. Protein side-chain atoms are colored according to chemical identity, with light green used for carbon, dark blue for nitrogen, red for oxygen, and yellow for sulfur. Labels are in light green for hydrophobic residues, dark blue for basic residues, and red for acidic residues. (A) Cavity map (27) of the nucleotide-free protomer. The cavities are shown by the magenta contours. The translucent gray boxes indicate the locations of the possible ligand-binding sites shown in (B), (C), and fig. S5. (B) The methionine canyon. (C) The COOH-terminal linker (CTL) binding groove. The CTL is shown in translucent red.

affinity ATPase site. The other PE sites are located in the PPXD or close to the COOH-terminus of SecA (figs. S2 and S3). One of the COOH-terminal sites is located in the Zn-binding domain that is disordered in the structure, but the other is located at the end of the CTL near the center of the SecA molecule (as shown in Fig. 1).

Although the PE sites are separated by as much as 80 Å in the protomer, they do cluster on one surface of SecA (Fig. 1), which is therefore likely to face SecYEG. Consistent with this conclusion, the most strongly conserved surfaces in the protomer are located in the vicinity of the PE sites on NBF-I, NBF-II, and the HSD. Furthermore, *in vitro* binding experiments show that epitopes in NBF-I and/or the PPXD make specific interactions

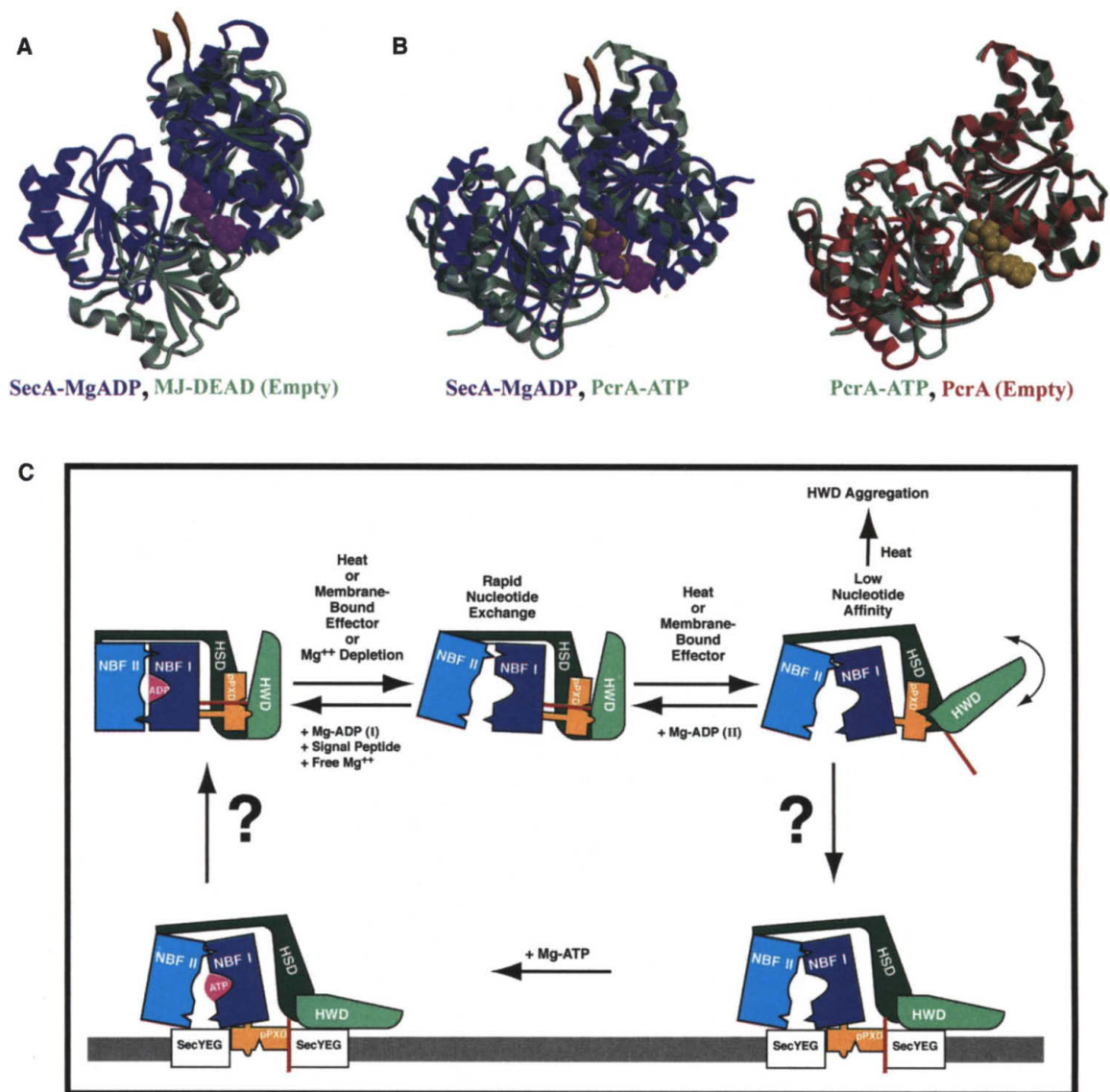
with SecYEG (39). However, segments of the HWD and HSD are also likely to interact with SecYEG, given the results of ligand-blotting experiments (40) combined with the fact that they form a 30-kD COOH-terminal protease-resistant fragment when SecA binds to SecYEG (1, 34, 41).

Neither of the PE sites in the PPXD is solvent-exposed in the crystal structure of *B. subtilis* SecA, consistent with the failure of Cys residues at these sites to react with thiol-reactive reagents in soluble *E. coli* SecA (38). One of these sites (Ser-330 in *B. subtilis*) is located in a rigorously conserved sequence that packs onto the surface of the HSD in a region of reliable electron density; exposure of this site to the periplasm requires an opening of the interface between the PPXD

and the HSD when SecA binds to SecYEG.

**Locations of potential ligand-binding sites.** SecA interacts with a variety of “translocation ligands,” including the preprotein translocation substrate (8, 9, 11, 12) and acidic phospholipids (37). A cavity map was calculated (21) to guide the search for potential ligand-binding sites in SecA, revealing one network of cavities at the interface between the PPXD and the HSD/HWD and a second network of cavities in the vicinity of the high-affinity ATPase site at the interface between NBF-I, NBF-II, and the HSD (Fig. 3A). The porous nature of the interface of the PPXD could contribute to its weak attachment to the core of SecA as evidenced by its high backbone *B* factors. Based on the results of the preprotein cross-linking experiments with overlapping fragments of SecA

**Fig. 4.** Proposed mechanism for the conformational reaction cycle of SecA. (A) and (B) compare the tandem motor domains in SecA to those in two structurally related ATP-dependent helicases based on least-squares alignment of NBF-I with the equivalent helicase domain. The nucleotide-binding core of SecA is shown in dark blue, with the  $\beta$  strands leading into and out of the preprotein-cross-linking domain shown in yellow and a space-filling model of the bound Mg-ADP shown in magenta. The motor domains from the related mechanoenzymes are shown in green or red, with their bound nucleotides shown as a yellow space-filling model when present. (Supplementary fig. S6 presents an equivalent comparison of the tandem motor domains in SecA with those in the  $\alpha/\beta$  heterodimer of the F1 ATPase and also of the nucleotide-free, Mg-ADP-bound, and Mg-AMPPNP-bound conformations of the  $\alpha/\beta$  heterodimer of F1.) (A) Comparison of SecA to the nucleotide-free structure of the SF-II DEAD-box helicase MJ0669 (30). (B) (Left) Comparison of SecA with the SF-I PcrA DNA helicase (29). (Right) Comparison of two conformations of PcrA (based on least-squares alignment of NBF-I), showing a significant opening of the ATPase active site at the interface between NBF-I and NBF-II in PcrA in the nucleotide-free conformation (red) compared with



the ATP-bound conformation (green). (C) The mechanistic schematic is colored according to domain organization as

(11), this porous interface of the PPXD represents a potential preprotein binding site. A second potential binding site is located in the network of cavities at the interface of NBF-I, NBF-II, and the HSD in a region designated the "methionine canyon" (Fig. 3, A and B). This weakly packed, methionine-rich, conserved hydrophobic interface between NBF-II and the NH<sub>2</sub>-terminus of  $\alpha$ -helix 1 in the HSD represents a potential binding site for either a phospholipid ligand or perhaps a preprotein. In the crystal, this cavity is only wide enough to accommodate a hydrocarbon moiety, but the high backbone *B* factors in this region raise the possibility that it could expand upon ligand binding. Another candidate preprotein binding site is the groove occupied by the CTL on the surface of NBF-I. SecA still functions when the CTL is genetically excised from this site in COOH-terminal deletion constructs (42). The CTL-binding groove is a highly conserved and largely hydrophobic surface at the interface between NBF-I and the  $\beta$  strand connecting it to the PPXD(N) (Fig. 3C). The phylogenetically conserved acidic environment surrounding this hydrophobic site is electrostatically complementary to the basic charge at the NH<sub>2</sub>-terminus of the signal sequence, making it an attractive binding site for this prototypical preprotein transport substrate. All three of these potential binding sites are located close to one or more PE epitopes (Fig. 1), so that a preprotein bound at any of them could be delivered to the pore of the

translocon when SecA binds to SecYEG (2, 3).

**Overlapping binding sites for the CTL and single-stranded nucleic acids.** Free cytoplasmic SecA attenuates the translation of its own mRNA based in part on sequence-specific RNA binding (43, 44). This autoregulatory activity mediates a reduction in SecA expression when there is an excess supply of the protein not actively engaged in protein translocation. DNA-bound structures of the SF-I helicases PcrA (29) and Rep (45) and the SF-II helicase NS3 (46) show a conserved single-stranded DNA (ssDNA)-binding groove at the interface between NBF-I and NBF-II. A groove of comparable geometry is preserved at the equivalent site in SecA (fig. S5), which could therefore interact with the adenine-rich ssRNA loop that is a putative regulatory target in SecA's mRNA (43). However, if preproteins were to occupy the CTL binding site (Fig. 3, A and C), they would probably prevent the binding of ssRNA to the adjacent groove and thereby inhibit any autogenous translational attenuation dependent on such an interaction (43).

**The physiological dimer.** The SecA crystals contain one protomer in the asymmetric unit, but one of the crystallographic dimers (Fig. 1B) is a strong candidate to be the physiological dimer (16, 47) based on the large magnitude of buried solvent-accessible surface area and the extensive number of intermolecular contacts. The PE sites and the potential preprotein binding sites are all lo-

cated on or near the front surface of this dimer (Fig. 1B). Although the COOH-terminal Zn-binding domains are disordered, their approximate positions can be inferred from the locations of the proximal protein segments (i.e., the COOH-termini of the CTL), which are located near the center of the dimer on this same surface. Therefore, both COOH-terminal Zn-binding domains probably project forward from this surface, where they could simultaneously interact with a single SecB tetramer (4, 36).

**Likely role of nucleotide binding to the high-affinity ATPase site.** Comparison of the conformation of the tandem motor domains in SecA to those in the crystal structure of its close structural homolog, the MJ0669 DEAD-box helicase (30), gives insight into the likely structural consequences of ATP binding to the high-affinity ATPase site. This site is markedly open in MJ0669 compared with SecA because of a 50° downward rotation of NBF-II relative to NBF-I (Fig. 4A). Although the structural consequences of nucleotide binding to MJ0669 have not been characterized experimentally, bringing the helicase motifs from NBF-II (including the Arg-finger) into position to encapsulate the nucleotide as they do in other helicase structures (e.g., as in Fig. 2C) would require a large relative rotation of the NBFs. A similar kind of nucleotide-dependent rotation of the NBFs, although of smaller magnitude, is observed when comparing the nucleotide-free and ATP-bound conformations of the SF-I PcrA helicase (29) (Fig. 4B). Very similar nucleotide-dependent mechanical changes are also observed in two other evolutionarily related mechanoenzymes, the gene 4 hexameric ring helicase (PDB accession number 1CR1) (18) and the  $\alpha/\beta$  heterodimer of F1 ATPase (27, 48) (fig. S6), both of which bind ATP at the interface between two nonidentical but homologous protein domains whose topology is the same as that of the NBFs in SecA. These observations show that the tandem NBFs in SF-I -II helicases and related mechanoenzymes function as an ATP-dependent mechanical clamp (25, 26).

The submicromolar affinity of soluble SecA for ADP and ATP- $\gamma$ -S (19), combined with the failure of nucleotide binding to cause a large conformational change (16), suggests that the ground-state conformation of *apo* SecA is very similar to that of the nucleotide-bound enzyme. This conclusion is consistent with the closed conformation of the high-affinity ATPase site observed in the crystal structure of SecA and its isomorphous crystallization either in the presence or absence of nucleotides. However, in one of the other conformational states in the mechanochemical reaction cycle of SecA (Fig. 4C), its high-affinity ATPase site may exist in an open configuration more like that observed

**Table 1.** *B. subtilis* SecA refinement statistics. Standard definitions were used for all parameters (21, 60). For the nucleotide-free (i.e., sulfate-bound) structure, the value of  $\langle I \rangle / \langle \sigma \rangle$  was 2.1 in the limiting-resolution shell, which was 100% complete for all measured reflections and 40% complete for reflections with  $I \geq 2\sigma$ . For the Mg-ADP-bound structure, the value of  $\langle I \rangle / \langle \sigma \rangle$  was 1.4 in the limiting-resolution shell, which was 100% complete for all measured reflections and 34.0% complete for reflections with  $I \geq 2\sigma$ .

Space group <i>P</i> 3 <sub>1</sub> 2			
	Sulfate	Mg-ADP	
Crystal parameters:			
Cell constants at 100 K	$a = b = 130.8 \text{ \AA}$ $c = 150.4 \text{ \AA}$	$a = b = 131.2 \text{ \AA}$ $c = 150.5 \text{ \AA}$	(90°, 90, 120°)
Data quality:			
Resolution	50.0–2.7 $\text{\AA}$	50.0–3.0 $\text{\AA}$	
$R_{\text{sym}}$	7.8%	7.4%	( $I \geq -3\sigma$ , for observations)
Mean redundancy	6.9	7.2	
Completeness	99.6%	99.8%	( $I \geq \sigma$ , after merging)
Mean $I/\sigma$	18.9	20.6	
Residuals ( $F \geq 2\sigma$ ):			
$R_{\text{free}}$	30.4%	29.4%	
$R_{\text{work}}$	22.1%	21.8%	
Model quality:			
rms bond lengths	0.013 $\text{\AA}$	0.013 $\text{\AA}$	
rms bond angles	1.74°	1.84°	
Ramachandran plot	83.3%	82.1%	Core
	14.4%	15.2%	Allowed
	2.1%	2.3%	Generously allowed
	0.3%	0.4%	Disallowed
Model contents:			
Protein residues	1–802	1–802	
Ligands	7 sulfates	1 Mg-ADP 5 sulfates	
Water molecules	45	46	

in nucleotide-free MJ0669 (30) (Fig. 4A), and this state would be expected to have significantly reduced nucleotide affinity owing to the inability of the helicase motifs in both NBFs to simultaneously interact with the nucleotide. The relative rotation of NBF-I and NBF-II that would produce such

an opening is likely to produce global changes in the domain-domain interactions in SecA given the network of cooperative inter-domain packing interactions in the protomer. Such a global conformational change could in turn gate interaction with translocation ligands owing to the exposure of new protein-

and ligand-binding sites on SecA (Fig. 4C).

There is in fact a well-characterized endothermic conformational transition in soluble SecA that has been hypothesized to gate membrane binding (20, 49–51). This transition is facilitated by SecA mutations that suppress secretion defects caused by muta-

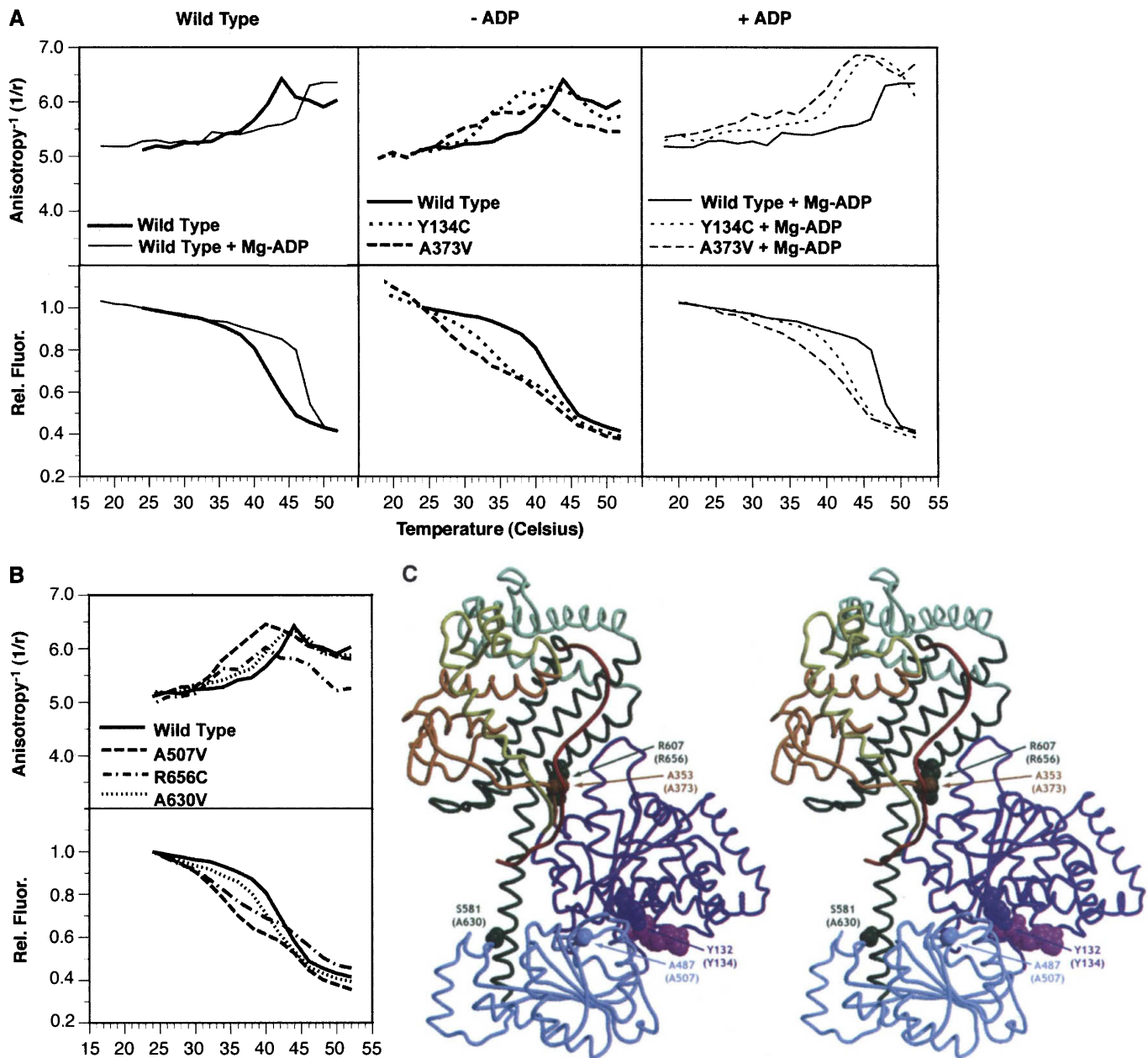


**Fig. 5.** Fluorescence anisotropy titrations of suppressor mutations in *E. coli* SecA. With the exception of A630V, all the mutations characterized here exhibit the *prID* phenotype (58, 59), defined by suppression of secretion defects caused by mutations in the signal sequence of the preprotein. The mutations also yield enhanced resistance to azide, except the A507V mutation, which yields hypersensitivity. The A373V and A507V mutations confer the “superactive” SecA phenotype (54). (A) Tryptophan fluorescence spectra (21) of the wild-type and two mutant proteins were acquired as a function of temperature in the presence and absence of 1.0 mM Mg-ADP. The bottom graphs show the relative total fluorescence ( $\| + 2\perp$ ), while the top graphs show Perin plots of

reciprocal steady-state anisotropy [ $(\| + 2\perp)/(\| - \perp)$ ]. Note that an increase in the Perin plot represents a decrease in anisotropy. (B) Tryptophan fluorescence spectra (21) of three additional suppressor mutations were acquired as a function of temperature in the absence of Mg-ADP. (C) Stereo pair showing the sites of the suppressor mutations in *E. coli* SecA. The side chains of the equivalent residues in *B. subtilis* SecA are shown in space-filling representations colored according to the domain of origin. The 54% sequence identity between the two proteins allows unambiguous identification of the corresponding residues. The residue numbers from the *E. coli* enzyme are given in parentheses.

tions in either the signal sequence of the preprotein or SecYEG (52). The temperature dependence of many mutant and suppressor phenotypes indicates a central role for an endothermic reaction in the transport process (50, 53, 54), which is likely to be the endothermic conformational transition of SecA given that ATP hydrolysis is exothermic.

Because nucleotide binding increases the enthalpy and  $T_m$  (midpoint temperature) of the endothermic transition (20, 49) (Fig. 5A), the high-temperature conformation must have reduced nucleotide affinity, suggesting that the transition produces a relative rotation of the NBFs leading to an opening of the active-site cleft (Fig. 4C) as observed in the nucleotide-free conformations of the structurally related mechanoenzymes (Fig. 4, A and B; fig. S6). The suppressor mutations that facilitate this endothermic transition in *E. coli* SecA map broadly over the interdomain interfaces in *B. subtilis* SecA (Fig. 5C), showing that local conformational changes take place simultaneously at these widely distributed sites coupled to the reduction in nucleotide affinity (as proposed in Fig. 4C).

**An increase in protein mobility during the endothermic transition.** Thermal titrations of several variants of *E. coli* SecA monitored by steady-state tryptophan (Trp) fluorescence anisotropy spectroscopy (Fig. 5, A and B) (21) indicate that an increase in protein mobility accompanies the endothermic transition, which was previously shown to produce a quenching in total fluorescence based primarily on increased solvent-exposure of Trp-775 (51). Quenching produces a reduction in fluorescence lifetime that, in the absence of other effects, tends to produce an increase in anisotropy owing to shortening of the time for rotational reorientation before photon emission. In contrast, the Perin plots (55) of reciprocal anisotropy versus temperature (Fig. 5, A and B) show a decrease in anisotropy coincident with the fluorescence quenching that can only be explained by an increase in the mobility (i.e., rotational diffusion coefficient) of the Trp ensemble in *E. coli* SecA during the endothermic transition. Many suppressor mutations that facilitate the endothermic transition split the single conformational transition in wild-type *E. coli* SecA into two different subtransitions (52), as observed in wild-type *B. subtilis* SecA (20). The anisotropy transition always coincides with the first endothermic subtransition in these *E. coli* SecA variants (Fig. 5, A and B). This first subtransition (but not the second) is fully reversible (56), showing that the associated increase in the mobility of the Trp ensemble occurs as part of a well-behaved conformational reaction.

This increase in mobility could result either from monomerization of the physiological dimer of SecA or from a domain-dissociation reaction in the protomer that would

allow a portion of the molecule to reorient itself more rapidly than the dimer. In either case, the first endothermic subtransition must involve disruption of domain-domain interactions observed in the native SecA dimer. If the increase in mobility is derived from monomerization, it would be expected to occur cooperatively in the two protomers. However, the reverse conformational reaction occurs independently in each protomer when driven by Mg-ADP titration (fig. S7), indicating that the increase in mobility during the forward reaction must also occur independently and therefore must be attributable to domain-dissociation within each individual protomer rather than monomerization. Using a complete set of single Trp-to-Phe mutations to dissect the anisotropy transition (fig. S8 and SOM text) suggests that the two Trp residues in the HWD are responsible for the increase in the mobility of the Trp ensemble. Therefore, the HWD must dissociate from the core of SecA during the first endothermic subtransition, coupled to a reduction in nucleotide-binding affinity of the ATPase site at the interface of the tandem NBFs near the distal end of the protomer (top of Fig. 4C).

#### Hypothesis for the mechanism of binding and release of SecA from SecYEG.

The occurrence of domain dissociation explains how the endothermic transition could gate the interaction of SecA with SecYEG (Fig. 4C). The HSD and HWD constitute the most protease-sensitive region of SecA at elevated temperatures (57) but form a highly protease-resistant structure when SecA binds to SecYEG (1, 34, 41), indicating that they make new structural interactions in the complex. The dissociation of the HWD, coupled to increased solvent exposure of the HSD [e.g., Trp-775 in *E. coli* SecA (51)], indicates that buried epitopes throughout these regions become exposed during the endothermic transition, which could thereby gate the binding of SecA to SecYEG if these newly exposed epitopes make contacts in the resulting complex.

Starting from the nucleotide-free domain-dissociated conformation, ADP binding to the high-affinity ATPase site in SecA reverses the domain-dissociation reaction and restores the compact conformational ground state with lower affinity for SecYEG (shown experimentally in fig. S7 and schematically at the top of Fig. 4C). The nucleotide probably acts by changing the packing angle between NBF-I and NBF-II so as to stabilize the network of cooperative interdomain packing interactions favoring this conformation.

The effects of ATP binding to the high-affinity ATPase site in SecA could be fundamentally similar to those of ADP binding to this site. In F1 ATPase,  $\alpha/\beta$  heterodimers with either ATP or ADP bound have a very similar conformation (fig. S6, right), but the thermodynamic stability of the ATP-bound

structure must be higher given the ability of F1 to drive the synthesis of ATP (27, 48). A similar mechanism could be used by SecA, with ATP and ADP binding to fundamentally similar conformations of the enzyme that differ primarily in their thermodynamic stability. In this case, ATP hydrolysis would serve to weaken the complex in order to facilitate nucleotide release (perhaps with the assistance of a membrane-bound nucleotide-release factor) and thereby shift the equilibrium to the domain-dissociated conformation with higher affinity for SecYEG (Fig. 4C, right side). If this hypothesis is correct, ATP binding to the high-affinity ATPase site could potentially drive the withdrawal of SecA from SecYEG when polypeptide transport is complete by stabilizing the compact conformation of SecA observed in the crystal structure (Fig. 4C, left side). Consistent with this possibility, mutations that impair the high-affinity ATP-binding site cause SecA to fractionate almost exclusively in the membrane-bound form (5). Although the ATP analog AMPPNP stabilizes the SecA complex with SecYEG (2, 10), it binds with three orders of magnitude lower affinity than ADP or ATP- $\gamma$ -S and therefore may act as an antagonist of ATP binding rather than as a mimic of the genuine ATP-bound state (20, 56). However, the structural mechanics of the processive polypeptide transport reaction are likely to be complex so that ATP binding and hydrolysis at this site could have more complicated effects when SecA is engaged with SecYEG (1, 3).

#### References and Notes

1. A. Economou, W. Wickner, *Cell* **78**, 835 (1994).
2. A. Economou, J. A. Pogliano, J. Beckwith, D. B. Oliver, W. Wickner, *Cell* **83**, 1171 (1995).
3. J. P. van der Wolk, J. G. de Wit, A. J. Driessen, *EMBO J.* **16**, 7297 (1997).
4. A. J. Driessen, E. H. Manting, C. van der Does, *Nature Struct. Biol.* **8**, 492 (2001).
5. T. Rajapandi, D. Oliver, *Mol. Microbiol.* **20**, 43 (1996).
6. R. J. Cabelli, L. Chen, P. C. Tai, D. B. Oliver, *Cell* **55**, 683 (1988).
7. R. Lill *et al.*, *EMBO J.* **8**, 961 (1989).
8. T. L. Triplett *et al.*, *J. Biol. Chem.* **276**, 19648 (2001).
9. C. Baud *et al.*, *J. Biol. Chem.* (2002).
10. E. Schiebel, A. J. Driessen, F. U. Hartl, W. Wickner, *Cell* **64**, 927 (1991).
11. E. Kimura, M. Akita, S. Matsuyama, S. Mizushima, *J. Biol. Chem.* **266**, 6600 (1991).
12. F. van Voorst, I. J. Vereyken, B. de Kruijff, *FEBS Lett.* **486**, 57 (2000).
13. S. Weinkauff *et al.*, *Acta Crystallogr. D* **57**, 559 (2001).
14. J. F. Hunt, J. Deisenhofer, in preparation.
15. K. Cowtan, P. Main, *Acta Crystallogr. D* **54**, 487 (1998).
16. B. Shilton *et al.*, *FEBS Lett.* **436**, 277 (1998).
17. C. Mitchell, D. Oliver, *Mol. Microbiol.* **10**, 483 (1993).
18. J. F. Hunt *et al.*, data not shown.
19. T. den Blaauwen, J. P. van der Wolk, C. van der Does, K. H. van Wely, A. J. Driessen, *FEBS Lett.* **458**, 145 (1999).
20. T. den Blaauwen, P. Fekkes, J. G. de Wit, W. Kuiper, A. J. Driessen, *Biochemistry* **35**, 11994 (1996).
21. Materials and methods are available as supporting material on Science online.
22. E. V. Koonin, A. E. Gorbalenya, *FEBS Lett.* **298**, 6. (1992).
23. G. Sianidis *et al.*, *EMBO J.* **20**, 961 (2001).
24. J. de la Cruz, D. Kressler, P. Linder, *Trends Biochem. Sci.* **24**, 192 (1999).

## RESEARCH ARTICLES

25. M. R. Singleton, D. B. Wigley, *J. Bacteriol.* **184**, 1819 (2002).
26. J. M. Caruthers, D. B. McKay, *Curr. Opin. Struct. Biol.* **12**, 123 (2002).
27. J. P. Abrahams, A. G. Leslie, R. Lutter, J. E. Walker, *Nature* **370**, 621 (1994).
28. L. Holm, C. Sander, *Trends. Biochem. Sci.* **20**, 478 (1995).
29. S. S. Velankar, P. Soultanas, M. S. Dillingham, H. S. Subramanya, D. B. Wigley, *Cell* **97**, 75 (1999).
30. R. M. Story, H. Li, J. N. Abelson, *Proc. Natl. Acad. Sci. U.S.A.* **98**, 1465 (2001).
31. E. R. Johnson, D. B. McKay, *RNA* **5**, 1526 (1999).
32. J. M. Caruthers, E. R. Johnson, D. B. McKay, *Proc. Natl. Acad. Sci. U.S.A.* **97**, 13080 (2000).
33. C. van der Does et al., *Mol. Microbiol.* **22**, 619 (1996).
34. J. Eichler, W. Wickner, *Proc. Natl. Acad. Sci. U.S.A.* **94**, 5574 (1997).
35. P. Fekkes, J. G. de Wit, A. Boorsma, R. H. Friesen, A. J. Driessen, *Biochemistry* **38**, 5111 (1999).
36. P. Fekkes, C. van der Does, A. J. Driessen, *EMBO J.* **16**, 6105 (1997).
37. E. Breukink et al., *J. Biol. Chem.* **270**, 7902 (1995).
38. V. Ramamurthy, D. Oliver, *J. Biol. Chem.* **272**, 23239 (1997).
39. V. Dapic, D. Oliver, *J. Biol. Chem.* **275**, 25000 (2000).
40. S. Snyders, V. Ramamurthy, D. Oliver, *J. Biol. Chem.* **272**, 11302 (1997).
41. C. van der Does, E. H. Manting, A. Kaufmann, M. Lutz, A. J. Driessen, *Biochemistry* **37**, 201 (1998).
42. T. Rajapandi, D. Oliver, *Biochem. Biophys. Res. Commun.* **200**, 1477 (1994).
43. R. Salavati, D. Oliver, *J. Mol. Biol.* **265**, 142 (1997).
44. H. Nakatogawa, K. Ito, *Mol. Cell* **7**, 185 (2001).
45. S. Korolev, J. Hsieh, G. H. Gauss, T. M. Lohman, G. Waksman, *Cell* **90**, 635 (1997).
46. J. L. Kim et al., *Structure* **6**, 89 (1998).
47. R. L. Woodbury, S. J. Hardy, L. L. Randall, *Protein Sci.* **11**, 875 (2002).
48. R. I. Menz, J. E. Walker, A. G. Leslie, *Cell* **106**, 331 (2001).
49. N. D. Ulbrandt, E. London, D. B. Oliver, *J. Biol. Chem.* **267**, 15184 (1992).
50. V. Ramamurthy, V. Dapic, D. Oliver, *J. Bacteriol.* **180**, 6419 (1998).
51. H. Ding, I. Mukerji, D. Oliver, *Biochemistry* **40**, 1835 (2001).
52. M. Schmidt, H. Ding, V. Ramamurthy, I. Mukerji, D. Oliver, *J. Biol. Chem.* **275**, 15440 (2000).
53. K. Nishiyama, T. Suzuki, H. Tokuda, *Cell* **85**, 71 (1996).
54. G. Matsumoto, H. Nakatogawa, H. Mori, K. Ito, *Genes Cells* **5**, 991 (2000).
55. J. R. Lakowicz, *Principles of Fluorescence Spectroscopy* (Plenum, New York, 1983).
56. J. J. Fak, J. Benach, A. Itkin, L. Gierasch, J. F. Hunt, in preparation.
57. M. Song, H. Kim, *J. Biochem.* **122**, 1010 (1997).
58. J. D. Fikes, P. J. Bassford Jr., *J. Bacteriol.* **171**, 402 (1989).
59. J. L. Huie, T. J. Silhavy, *J. Bacteriol.* **177**, 3518 (1995).
60. J. Drenth, *Principles of Protein X-ray Crystallography* (Springer-Verlag, New York, 1994).
61. We thank T. Rajapandi for construction of the N96C mutant of *B. subtilis* SecA; H. Ding for advanced access to the single-tryptophan substitution mutants of *E. coli* SecA; and M. Machius, D. Xia, R. Krishnaraj, and other members of the Deisenhofer, Sprang, and Goldsmith lab groups for advice and for assistance with crystallographic data collection. We also thank W. Hendrickson for a critical review of the manuscript and L. Gierasch, G. Wittrock, R. Chou, A. Driessen, T. Economu, and B. DeKruiff for insightful conversations. We acknowledge support during synchrotron data collection from M. Capel, T. Langdon, and C. Ogata of the National Synchrotron Light Source (NSLS); W. Miller, M. Szebenyi, and D. Thiel of Cornell High Energy Synchrotron Source (CHESS); and A. Thompson and B. Rasmussen of the European Synchrotron Radiation Facility (ESRF). We particularly thank A. Weaver and R. Cabelli for their pioneering efforts in initiating this project using *E. coli* SecA. The Howard Hughes Medical Institute supported this project in J.D.'s laboratory, and a startup grant from Columbia University and a grant from NIH General Medical Sciences supported the continuation of this project in J.F.H.'s laboratory. Coordinates and structure factors for the nucleotide-free and Mg-ADP-bound structures have been deposited in the PDB under accession codes 1M6N and 1M74, respectively.

### Supporting Online Material

[www.sciencemag.org/cgi/content/full/297/5589/2018/DC1](http://www.sciencemag.org/cgi/content/full/297/5589/2018/DC1)

Materials and Methods

SOM Text

Figs. S1 to S8

References and Notes

28 May 2002; accepted 5 August 2002

## REPORTS

# Physical One-Way Functions

Ravikanth Pappu,\*† Ben Recht, Jason Taylor, Neil Gershenfeld

Modern cryptographic practice rests on the use of one-way functions, which are easy to evaluate but difficult to invert. Unfortunately, commonly used one-way functions are either based on unproven conjectures or have known vulnerabilities. We show that instead of relying on number theory, the mesoscopic physics of coherent transport through a disordered medium can be used to allocate and authenticate unique identifiers by physically reducing the medium's microstructure to a fixed-length string of binary digits. These physical one-way functions are inexpensive to fabricate, prohibitively difficult to duplicate, admit no compact mathematical representation, and are intrinsically tamper-resistant. We provide an authentication protocol based on the enormous address space that is a principal characteristic of physical one-way functions.

Information security requires a mechanism that provides significant asymmetry in the effort required to make intended and unintended uses of encoded information. Such protection is growing in importance as an increasing fraction of economic activity is communicated electronically; sending credit card numbers over the Internet or spending money stored in a smart card's memory assumes

that these data cannot easily be duplicated.

Modern cryptographic practice rests on the use of one-way functions. These are functions that are easy to evaluate in the forward direction but infeasible to compute in the reverse direction without additional information. For example, multiplying large prime numbers can be done in a time that is a polynomial function of their size, but finding the prime factors of the product is believed to require exponential time (*1*). Another important example is the ease of modular exponentiation (evaluating  $a = b^c \pmod d$  for integers  $b$ ,  $c$ , and  $d = 2p + 1$ , where  $d$  and  $p$  are large primes) versus the difficulty of taking discrete logarithms (find-

ing the integer  $c$ , given  $a$ ,  $b$ , and a prime  $d$ ) (*2*).

Cryptographic applications that have variable-length inputs, such as storing computer passwords (*3*) or digitally signing secure electronic documents (*4*), use one-way hash functions as a cryptographic primitive. A hash function compresses an arbitrary-length input to a fixed-length output and has the avalanche property that changing one bit in the input flips roughly half the bits in the output. A one-way hash function has preimage resistance (it is infeasible to find an input that produces a given output), and it can also have collision resistance (it is difficult to find two inputs that produce the same output).

Although algorithmic one-way functions are widely used, they are facing a number of challenges. The first is technological, as massively parallel networks of computers break codes that had been considered safe (*5*) and secure processors containing keys are reverse-engineered (*6*). The second is fundamental, because the cryptographic primitives used are believed to be secure, but there is no proof that efficient attacks don't exist. Such attacks are in fact known using quantum computers; it is shown in (*7*) that factoring the product of two large prime numbers can be accomplished in polynomial time on a quantum computer. The third and perhaps most serious challenge is practical: The demands placed on the physical embodiments

Center for Bits and Atoms, The MIT Media Labs, 20 Ames Street, Cambridge, MA 02139, USA.

\*Present address: ThingMagic, One Broadway, 14th Floor, Cambridge, MA 02142, USA.

†To whom correspondence should be addressed. E-mail: ravi@thingmagic.com